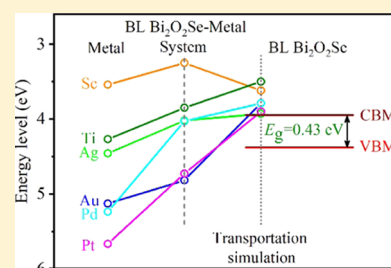


Pervasive Ohmic Contacts in Bilayer Bi₂O₂Se–Metal InterfacesLianqiang Xu,^{†,‡,⊙} Shiqi Liu,^{†,⊙} Jie Yang,[‡] Bowen Shi,[‡] Yuanyuan Pan,[‡] Xiuying Zhang,^{‡,⊙} Hong Li,[§] Jiahuan Yan,[‡] Jingzhen Li,[‡] Linqiang Xu,[‡] Jinbo Yang,^{*,‡,||} and Jing Lu^{*,‡,||}[†]School of Physics and Electronic Information Engineering, Engineering Research Center of Nanostructure and Functional Materials, Ningxia Normal University, Guyuan, Ningxia 756000, P. R. China[‡]State Key Laboratory of Mesoscopic Physics and Department of Physics, Peking University, Beijing 100871, P. R. China[§]College of Mechanical and Material Engineering, North China University of Technology, Beijing 100144, P. R. China^{||}Collaborative Innovation Center of Quantum Matter, Beijing 100871, P. R. China

ABSTRACT: Due to their outstanding gate electrostatics, two-dimensional (2D) semiconducting materials are regarded as promising channel materials used in the next-generation field-effect transistors (FETs). However, a Schottky barrier often existing at the 2D semiconductor–metal interface can evidently degrade the device performance. Very lately, 2D layered semiconducting bismuth oxyselenide (Bi₂O₂Se) is synthesized and exhibits high carrier mobility and excellent air stability. We conduct a systematic exploration, for the first time, on the interfacial nature of bilayer (BL) Bi₂O₂Se in contact with six metals (Sc, Ti, Ag, Au, Pd, and Pt) that cover a wide work function range by density functional theory-based band structure calculations and quantum transport simulations in a FET configuration. Remarkably, our results reveal that all the contacts in the lateral direction are n-type Ohmic due to the robust beyond-gap Fermi level pinning at the interface. Experimentally, the actual BL Bi₂O₂Se FET with a Au/Pd electrode indeed shows an n-type Ohmic contact. Hence, low contact resistance can easily be expected in BL Bi₂O₂Se devices.



1. INTRODUCTION

In recent years, many research studies have proved that two-dimensional (2D) semiconducting materials can effectively suppress the short-channel effects in field-effect transistors (FETs) owing to atomically thin uniform thickness and dangling-bond-free lateral pristine surfaces.^{1–9} Thus, 2D semiconducting materials are regarded as very promising candidate channel materials for using them in the next decade electronic and optoelectronic devices.^{1,3,6,7,9–12} In a practical FET with a 2D semiconductor as the channel material, however, the semiconductor–metal contact is commonly required for the carrier injection due to the absence of an effective substitutional doping scheme for 2D materials.^{1,7,9,12–15} A Schottky barrier (SB) usually emerging at the interface of the semiconductor–metal can remarkably lower the carrier injection efficiency and significantly deteriorate the FET performance.^{6,13,16,17} Therefore, to enhance the device performance, it is essential to effectively decrease the contact resistance or seek the Ohmic contact at the semiconductor–metal interfaces for the upcoming 2D FETs.^{14–16,18–27}

Most recently, the 2D layered bismuth oxyselenide (Bi₂O₂Se) crystal, which has a body-centered tetragonal structure composed of alternately arranged insulating [Bi₂O₂]²⁺ layers and conducting [Se]^{2–} layers, was discovered via an artful and low-cost chemical vapor deposition protocol.^{28–30} As a new star material, the 2D atomically thin Bi₂O₂Se film has superb properties, such as outstanding air stability, the layer-dependent bandgap (0.35–1.34 eV), ultrahigh electron Hall mobility (about 450 cm² V^{–1} s^{–1} at

300 K and 3 × 10⁵ cm² V^{–1} s^{–1} at 1.9 K), and remarkable structure stability under pressure (up to 30 GPa).^{28,29,31,32} Furthermore, it has been evidenced that the 2D Bi₂O₂Se-based top-gated FETs with the Pd/Au metal electrode exhibit superior current *I*_{on}/*I*_{off} ratios (larger than 10⁶) and a nearly ideal subthreshold swing (about 65 mV dec^{–1} at 300 K).²⁹ Hence, as a competitive channel material, 2D Bi₂O₂Se is anticipated to hold great potential applications in future high-performance (HP) and low-power (LP) digital logic nano-devices.²⁹ In addition, it should be noted that 2D Bi₂O₂Se also displays exceptional thermoelectricity,^{33–35} photoresponsivity,^{36–39} piezoelectricity, and ferroelectricity.⁴⁰ However, at present, a comprehensive understanding about the nature of the 2D Bi₂O₂Se–metal contacts is still lacking. Consequently, to fill the gap, it is imperative to implement a systematic investigation of 2D Bi₂O₂Se–metal interfaces.

The bilayer (BL) Bi₂O₂Se can be regarded as the simplest multilayer Bi₂O₂Se. In this paper, we carry out a systematic exploration on the interfacial properties of BL Bi₂O₂Se contacting with various metals (Sc, Ti, Ag, Au, Pd, and Pt) spanning a broad work function scope in a FET geometry for the first time. To achieve this goal, first-principles-based electronic structure computations and quantum transport simulations are employed to analyze the Schottky barrier height (SBH) and contact polarity. It is found that in the

Received: December 21, 2018

Revised: March 12, 2019

Published: March 15, 2019

vertical direction, electronic structure computations reveal that the SB and tunneling barrier (TB) are absent at the interface of the BL Bi₂O₂Se–metal contact owing to the intensive band hybridization; in the lateral direction, quantum transport simulations unmask that the n-type Ohmic contacts are always formed at the interface between the BL Bi₂O₂Se–metal system and channel BL Bi₂O₂Se. It should be highlighted that the simulated results of the BL Bi₂O₂Se and Au/Pd contact are in good agreement with the present experimental conclusion.²⁹ Our calculated results indicate that the interface of BL Bi₂O₂Se and the investigated metal tends to form a (quasi) Ohmic contact, and BL Bi₂O₂Se is a distinguished candidate channel material for the forthcoming sub-5 nm technology nodes.

2. METHODOLOGY

2.1. Interface Modeling. The optimized crystal structure of BL Bi₂O₂Se, which is composed of alternately arranged two buckled [Bi₂O₂]²⁺ layers and three planar [Se]²⁻ layers, is shown in Figure 1a,b. To balance the nonstoichiometry

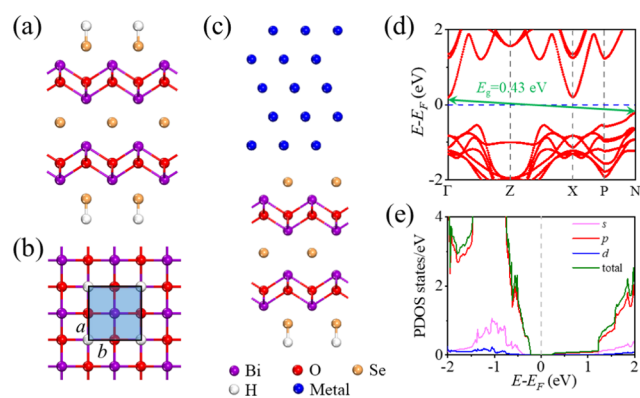


Figure 1. (a) Side and (b) top views of freestanding BL Bi₂O₂Se. Square indicates the unit cell of BL Bi₂O₂Se. (c) Initial geometry of the BL Bi₂O₂Se–metal (blue ball) interface. (d, e) Band diagram and partial density of states (PDOS) of intrinsic BL Bi₂O₂Se, respectively.

resulting from the additional [Se]²⁻ layer, the two outermost [Se]²⁻ layers are passivated with H atoms. The relaxed lattice constant of the Bi₂O₂Se bilayer is *a* = *b* = 3.981 Å, which is in agreement with the reported results.^{29,33} As displayed in Figure 1d, the BL Bi₂O₂Se terminated with H atoms has an indirect bandgap of 0.43 eV with the absence of spin–orbital coupling at the density functional theory (DFT) level, which is consistent with the previous study.²⁹ The valence band maximum (VBM) is located at the Γ point and the conduction band minimum (CBM) is located at the N point, which is in accordance with the former report.³¹ It should be emphasized that BL Bi₂O₂Se has a body-centered tetragonal Brillouin zone (BZ),³¹ rather than the simple tetragonal BZ adopted in several simulations about Bi₂O₂Se.^{29,40} From the projected density of states (PDOS) of BL Bi₂O₂Se exhibited in Figure 1e, it can be observed that the states near the CBM and VBM mainly originate from the p orbital of BL Bi₂O₂Se.

We employ six metals Sc, Ti, Ag, Au, Pd, and Pt, which involve a broad scope of work functions, and BL Bi₂O₂Se to construct the 2D semiconductor–metal interfacial system. As illustrated in Figure 1d, the BL Bi₂O₂Se–metal interfacial system is composed of five-layer metal atoms and BL Bi₂O₂Se, and the top two layers of metal atoms are fixed in the process of structure optimization. In the process of building the BL

Bi₂O₂Se–metal interfacial system, the lattice parameter of six metals is changed to match that of BL Bi₂O₂Se, and a vacuum buffer space of not less than 20 Å is added in the erect direction of the BL Bi₂O₂Se–metal interface. The $2 \times \sqrt{5}$ BL Bi₂O₂Se matches 3×3 Ag and Au surfaces in the (111) orientation, the $3 \times \sqrt{2}$ BL Bi₂O₂Se matches $2 \times \sqrt{21}$ Pd and Pt surfaces in the (111) orientation, the $\sqrt{2} \times \sqrt{5}$ BL Bi₂O₂Se matches the $\sqrt{7} \times \sqrt{3}$ Sc surface and the $\sqrt{2} \times \sqrt{10}$ BL Bi₂O₂Se matches the $\sqrt{3} \times \sqrt{19}$ Ti surface in the (0001) orientation, respectively. The mismatches between the six metals and BL Bi₂O₂Se are 1.28–5.97%, as shown in Table 1.

Table 1. Calculated Properties of BL Bi₂O₂Se–Metal Interfaces^a

	Ag	Au	Pd	Pt	Sc	Ti
$\bar{\epsilon}$ (%)	4.59	4.60	5.45	5.97	1.28	5.05
<i>d_z</i> (Å)	2.20	2.31	1.84	1.93	2.00	1.84
<i>d_{min}</i> (Å)	2.53	2.52	2.39	2.41	2.61	2.60
<i>E_b</i> (eV)	2.67	2.55	4.02	4.66	4.36	5.25
<i>W_M</i> (eV)	4.46	5.13	5.24	5.67	3.54	4.27
<i>W_S</i> (eV)	4.02	4.82	4.03	4.72	3.25	3.85
$\Phi_{L,W}^e$ (eV)	0.07	0.87	0.08	0.77	−0.70	−0.10
$\Phi_{L,W}^h$ (eV)	0.36	−0.44	0.35	−0.34	1.13	0.53
$\Phi_{L,T}^e$ (eV)	−0.02	−0.16	−0.16	−0.05	−0.33	−0.45
$\Phi_{L,T}^h$ (eV)	0.37	0.42	0.38	0.55	0.82	0.85
<i>E_g^T</i> (eV)	0.35	0.26	0.22	0.50	0.49	0.40

^a $\bar{\epsilon}$ stands for the mean lattice constant mismatch of the BL Bi₂O₂Se–metal interface. *d_z* stands for the mean distance of the BL Bi₂O₂Se–metal interface along the vertical direction. *d_{min}* stands for the minimum interatomic distance of the BL Bi₂O₂Se–metal interfaces. The binding energy *E_b* stands for the energy per BL bismuth oxytelluride unit required to remove BL Bi₂O₂Se from the metal surface. *W_M* and *W_S* stand for the calculated WF of the clean metal surface and the BL Bi₂O₂Se–metal system, respectively. $\Phi_{L,W}^e$ ($\Phi_{L,W}^h$) and $\Phi_{L,T}^e$ ($\Phi_{L,T}^h$) stand for the lateral electron (hole) SBHs calculated using the work function approximation method and the quantum transport simulation approach, respectively. *E_g^T* stands for the transmission gap of the BL Bi₂O₂Se FETs.

2.2. Band Structure Calculations. The structure relaxations, band structures, and DOS of the BL Bi₂O₂Se crystal and the BL Bi₂O₂Se–metal interfacial system are calculated using the Vienna ab initio simulation package.^{41,42} The plane-wave basis sets⁴³ with a cutoff energy of 500 eV, projected augmented wave pseudopotential,^{44,45} and generalized gradient approximation (GGA) of Perdew–Burke–Ernzerhof (PBE) functional^{46,47} are chosen in this study. The convergence tolerance for the residual force and total energy are, respectively, set to not more than 0.02 eV Å^{−1} and 10^{−5} eV/atom. The *k*-mesh density based on the Monkhorst–Pack scheme⁴⁸ is adapted to less than 0.02 Å^{−1} in the Brillouin zone sampling. Both van der Waals (vdW) interaction at the DFT-D3 level^{49–51} and dipole correction are also considered in all calculations.

2.3. Quantum Transport Simulations. To comprehensively examine the interfacial properties of BL Bi₂O₂Se–metal contact via quantum transport simulations, we design a two-probe FET model (Figure 2), which is composed of the optimized BL Bi₂O₂Se–metal interfacial system (used as an electrode) and intrinsic BL Bi₂O₂Se with a length of about 5 nm (used as a channel material). The two electrodes (left and right) of the FET model are semi-infinite, and the types of

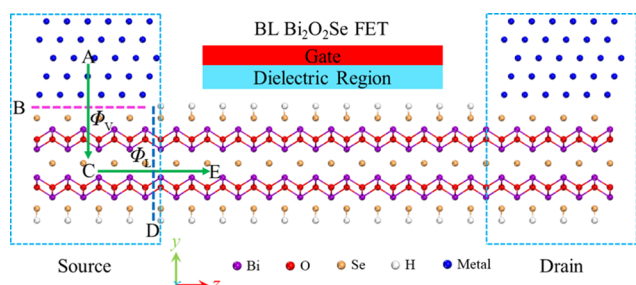


Figure 2. Schematic diagram of a single-gated BL Bi₂O₂Se FET. A, C, and E denote the three carrier (electron/hole) transfer regions. B denotes the source or drain interface (pink dashed line) and D stands for the source/drain-channel interface (blue dashed line). Φ_V represents the vertical SBH and Φ_L denotes the lateral SBH.

boundary conditions along the x , y , and z directions are set as periodic, Neumann, and Dirichlet, respectively. According to the previous results, a 2D semiconducting FET with a channel length of ~ 5 nm can well satisfy the purpose of evaluating SBH and contact polarity in a FET scheme.^{15,52,53}

The transmission coefficient and local device density of states (LDDOS) of the two-probe FET model constructed above under zero bias-voltage and gate-voltage are simulated via ab initio quantum transport simulations, which is based on DFT combined with the nonequilibrium Green's function (NEGF) method and implemented in the Atomistix ToolKit (ATK) 2017.12 package.^{54–56} The transmission coefficient $T(E)$ is derived from the mean value of k -dependent transmission coefficients $T^{k||}(E)$ through the Brillouin zone, and the $T^{k||}(E)$ at energy E can be defined as

$$T^{k||}(E) = \text{Tr}[\Gamma_L^{k||}(E)G^{k||}(E)\Gamma_R^{k||}(E)(G^{k||}(E))^\dagger] \quad (1)$$

In Formula 1, the $G^{k||}(E)$ ($G^{k||}(E)$)[†] stands for the retarded (advanced) Green function, and the $\Gamma_{L(R)}^{k||}(E) = i(\sum_{L(R)}^{k||} - (\sum_{L(R)}^{k||})^\dagger)$ represents the level broadening stemming from the left (right) electrode that is depicted by the electrode self-energy $\sum_{L(R)}^{k||}$.^{56,57} The functional with the GGA–PBE form, single- ξ polarized (SZP) basis set, real-space mesh cutoff of 75 Hartree, and electrode temperature of 300 K are adopted throughout the whole calculations. The Monkhorst–Pack-based k -point sampling in the electrode and the central region of a FET model are $10 \times 1 \times 100$ and $10 \times 1 \times 1$, respectively.

It is important to address that, in the light of the published works, the single- ξ polarized (SZP) basis set is usually sufficiently accurate for the systems of bulk metal used as the electrode.⁵⁸ And, for a FET based on a 2D semiconductor, the doped carriers originating from the metal electrode can greatly shield the electron–electron interaction in the channel. Consequently, the DFT–GGA strategy-based single electron approximation is effective enough to describe the electron behavior of the heavily doped 2D semiconductor and evaluate the SBH in a FET configuration, comparing with the results of the GW method and experiment.⁵⁹ For instance, at the DFT–GGA level, the calculated bandgap is 1.53 eV for a doped degenerately ML MoSe₂, which is in good agreement with the results of the GW method (1.59 eV) and experiment (1.58 eV);⁶⁰ the calculated electron (hole) SBH for the monolayer/bilayer/trilayer black phosphorene FET using Ni as the electrode is 0.39 (0.26)/0.52 (0.19)/0.48 (0.20) eV,^{15,61,62} which is also consistent with the experimental value of 0.64 (0.35)/0.48 (0.23)/0.40 (0.21) eV.⁶³

3. RESULTS AND DISCUSSION

3.1. Geometries and Electronic Structures. The relaxed BL Bi₂O₂Se–metal interfacial systems are presented in Figure 3. The positions of atoms at the BL Bi₂O₂Se–metal interface

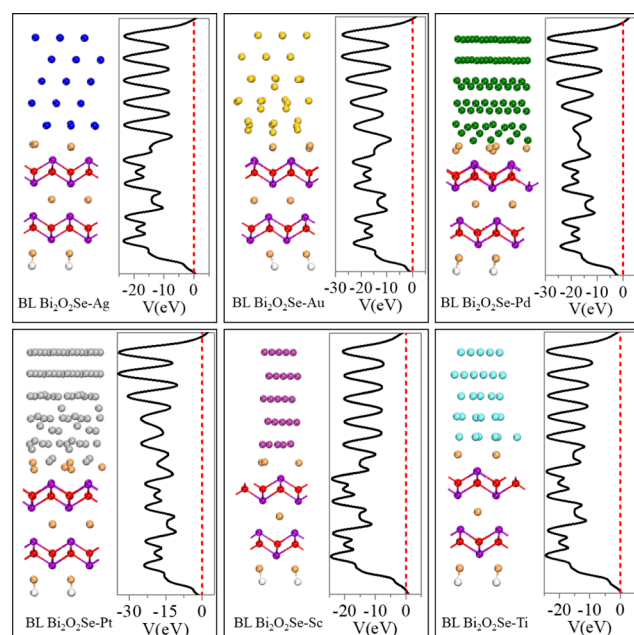


Figure 3. Side view of the relaxed architectures and mean electrostatic potential distribution in planes perpendicular to the BL Bi₂O₂Se–metal (Ag, Au, Pd, Pt, Sc, and Ti) interfaces. Fermi level is set as zero. Purple, red, brown, and white balls represent Bi, O, Se, and H atoms, respectively.

are strongly changed due to the intensive interaction of BL Bi₂O₂Se and the metal surface. In this work, we define three parameters, such as the binding energy (E_b), average distance (d_z), and minimum interatomic distance (d_{\min}), to better understand the interaction between BL Bi₂O₂Se and metal surfaces. The binding energy E_b of BL Bi₂O₂Se–metal interfacial systems is defined as

$$E_b = (E_{\text{BL Bi}_2\text{O}_2\text{Se}} + E_M - E_S)/N$$

where $E_{\text{BL Bi}_2\text{O}_2\text{Se}}$, E_M , and E_S stand for the total energy of the intrinsic BL Bi₂O₂Se, the clean metal surface, and the BL Bi₂O₂Se–metal interfacial systems, respectively. N represents the total number of BL Bi₂O₂Se unit cell, as shown in Figure 1b. d_z is the mean distance between BL Bi₂O₂Se and contacted metal along the vertical direction of the BL Bi₂O₂Se–metal interface, and d_{\min} is the minimum atomic distance of the selenium atom to the metal atom, as presented in Figure 1c. The calculated parameters including E_b , d_z , and d_{\min} are listed in Table 1. The binding energy E_b of BL Bi₂O₂Se contacting with Ag (2.67 eV) and Au (2.55 eV) is apparently smaller than that of BL Bi₂O₂Se contacting with Pd (4.02 eV), Pt (4.66 eV), Sc (4.36 eV), and Ti (5.25 eV); correspondingly, the interlayer distance d_z of BL Bi₂O₂Se–Ag (2.20 Å) and –Au (2.31 Å) contact is obviously larger than that of BL Bi₂O₂Se–Pd (1.84 Å), –Pt (1.93 Å), –Sc (2.00 Å), and –Ti (1.84 Å) contact. In spite of this, the values of E_b and d_z still give rise to strong bonding at the interface of the BL Bi₂O₂Se–metal contact, which can be further verified in the following analyses.

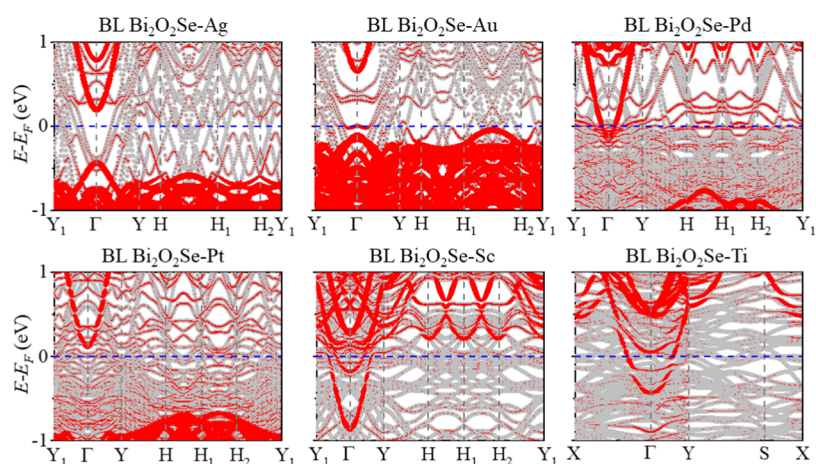


Figure 4. Band diagrams of BL Bi₂O₂Se–metal (Ag, Au, Pd, Pt, Sc, and Ti) systems. Gray and red lines represent band structures of the interfacial system and band structures projected to BL Bi₂O₂Se, respectively. The Fermi level is set as zero and denoted by a dashed blue line.

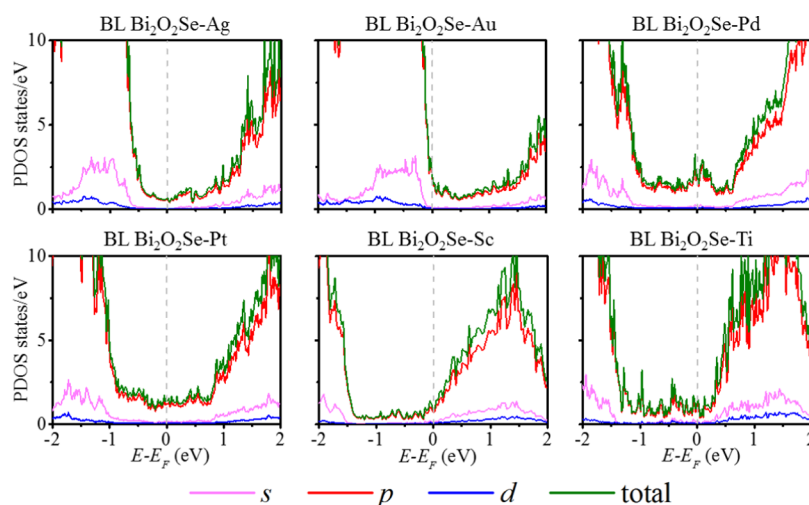


Figure 5. Partial density of states (PDOS) of BL Bi₂O₂Se–metal (Ag, Au, Pd, Pt, Sc, and Ti) systems. Fermi level is set as zero and denoted by dashed little-gray lines.

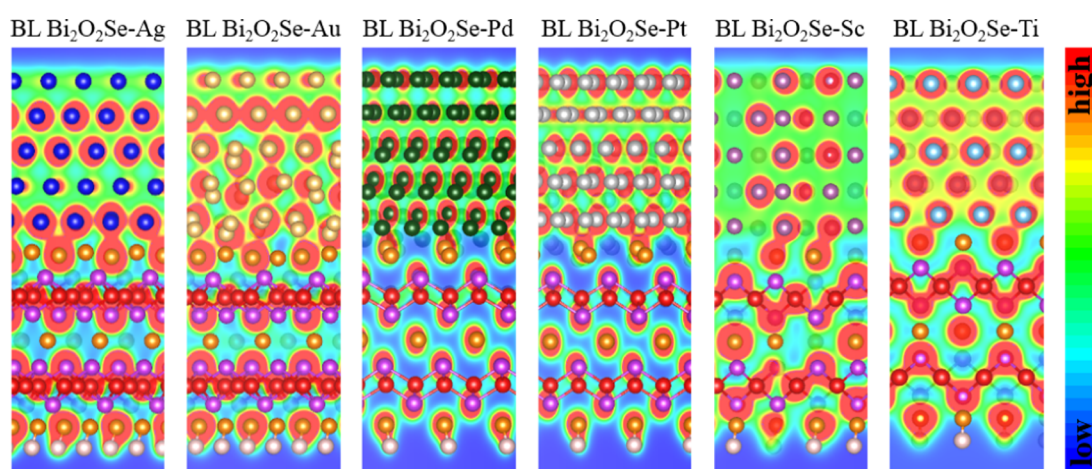


Figure 6. Total electron density distributions of the BL Bi₂O₂Se–metal (Ag, Au, Pd, Pt, Sc, and Ti) systems. Purple, red, brown, and white balls represent Bi, O, Se, and H atoms, respectively.

To gain better insight into the interaction strength between BL Bi₂O₂Se and the checked metals, we calculate the energy band structures, partial density of states (PDOS) projected onto BL Bi₂O₂Se, and total electron distribution of BL

Bi₂O₂Se–metal interfacial systems and show the analyzed results in Figures 4, 5, and 6, respectively. As shown in Figure 4, the band structure of BL Bi₂O₂Se is intensively destroyed and the Fermi level passes through the BL Bi₂O₂Se-derived

bands all the time, indicating strong band hybridization and metallization of BL Bi₂O₂Se in the examined BL Bi₂O₂Se–metal systems. Correspondingly, a great deal of gap states originating from BL Bi₂O₂Se spreads all over the band gap of intrinsic BL Bi₂O₂Se, as illustrated in Figure 5.

As shown in Figure 6, there is notable electron accumulation in the considered BL Bi₂O₂Se–metal interface region, suggesting the formation of a robust covalent bonding between BL Bi₂O₂Se and the metal surface. All the analytic results above clearly indicate that the BL Bi₂O₂Se absorbed on Ag, Au, Pd, Pt, Sc, and Ti substrates undergoes a forceful metallization and strong covalent bonds are formed at the interface of the BL Bi₂O₂Se–metal contact. Therefore, the vertical Schottky barrier (which may exist at interface B in Figure 2) is absent, and the corresponding Schottky barrier height (SBH), Φ_v , is zero due to the intensive metallization between BL Bi₂O₂Se and all the investigated metals. It is noteworthy that the interfaces between BL Bi₂O₂Se and the surveyed six metals all form the favorable Ohmic contact. So, a high efficiency of carrier injection can be anticipated when Ag, Au, Pd, Pt, Sc, and Ti are used as electrode metals to contact BL Bi₂O₂Se.

The other important potential barrier, namely the tunneling barrier (TB) that can also greatly influence the electrical characteristic of a 2D semiconductor–metal interface, may occur at interface B (as shown in Figure 2). To assess the TB of the BL Bi₂O₂Se–metal interface, we plot the electrostatic potential distribution of the studied 2D semiconductor–metal interfacial systems. As shown in Figure 3, the TB vanishes at the BL Bi₂O₂Se–Ag, Au, Pd, Pt, Sc, and Ti interfaces owing to the drastic metallization of BL Bi₂O₂Se. The absence of SB and TB at the checked BL Bi₂O₂Se–metal interface indicates that electrons can easily flow from the investigated metals to the contacted BL Bi₂O₂Se.

3.2. Lateral SBH Analysis. In a BL Bi₂O₂Se FET model, the SB may exist at interface B (the vertical SB) and D (the lateral SB), as shown in Figure 2. Based on the above analyses, the vertical SBH is zero for all the checked BL Bi₂O₂Se–metal interface. At present, there are two methods, work function approximation (WFA) and quantum transport calculation, that can be used to evaluate the lateral SBH of interface D. By means of the WFA, the lateral electron SBH ($\Phi_{L,W}^e$) (hole SBH ($\Phi_{L,W}^h$)) can be derived from the difference between the CBM (VBM) of the intrinsic BL Bi₂O₂Se and the Fermi level of the BL Bi₂O₂Se–metal interfacial system, and the computed results are shown in Table 1. At the WFA level, two lateral n-type Ohmic contacts are formed at interface D (Figure 2) when Sc and Ti are used as electrodes, two lateral p-type Ohmic contacts are found as Au and Pt are employed as electrodes, and two n-type quasi Ohmic contacts are generated with the electron (hole) SBHs of 0.06 (0.37) and 0.07 (0.36) eV, respectively, while Ag and Pd are chosen as electrodes. The SBH results obtained from the WFA method are illustrated in Figure 7. It is noteworthy that the coupling between the electrode region and the channel region is ignored in the WFA strategy.

To overcome the deficiency of the WFA scheme, a more reliable protocol named quantum transport calculation, which takes the electrode–channel coupling into account, is adopted to evaluate the lateral SBH at interface D (Figure 2) in a two-probe FET model with the channel length of about 5 nm.^{15,52,53,61} In the quantum transport calculation, the LDDOS in the BL Bi₂O₂Se FET, which directly depicts the distribution of the metal-induced-gap states (MIGS) and the

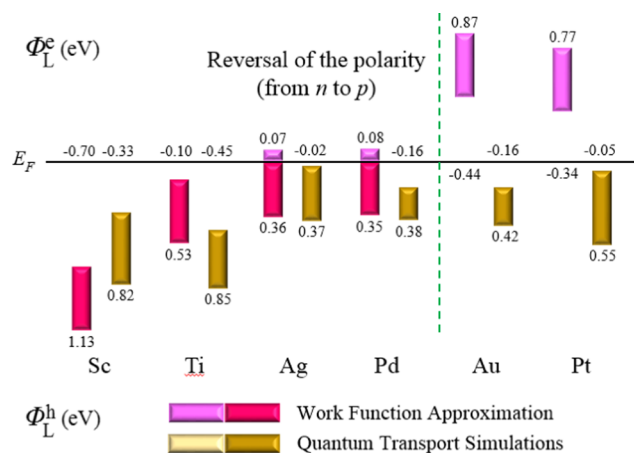


Figure 7. Comparison of the lateral SBHs obtained from the WFA and the quantum transport simulations for the BL Bi₂O₂Se FET.

real-space energy band in a FET, is used to analyze the lateral electron (hole) SBH that is quantitatively obtained from the difference of the CBM (VBM) and the Fermi level of the channel BL Bi₂O₂Se at interface D (Figure 2). The LDDOS and its corresponding transmission spectrum in the BL Bi₂O₂Se FET are shown in Figure 8. It should be noted that the average SBH of the left and right interface is adopted if the lateral electron (hole) SBH is not equal at the two interfaces.^{15,61–63} For instance, the left and right lateral electron (hole) SBHs of the BL Bi₂O₂Se FET with the Ag electrode are 0.11 (0.25) eV and -0.14 (0.49) eV, respectively, and the average lateral electron (hole) SBH of -0.02 (0.37) eV is obtained. After careful analysis, six lateral n-type Ohmic contacts are formed at interface D (Figure 2) when the checked six metals are used as electrodes in a FET model. Therefore, low contact resistance is anticipated in the BL Bi₂O₂Se-based FETs using Ag, Au, Pd, Pt, Sc, and Ti as the electrodes. The analytic results of the lateral electron (hole) SBH $\Phi_{L,T}^e$ ($\Phi_{L,T}^h$) derived from the quantum transport calculation strategy are also displayed in Figure 7 and compared with those obtained from the WFA method. It is important to note that the formation of n-type Ohmic contact at BL Bi₂O₂Se–Pd and BL Bi₂O₂Se–Au interfaces is well consistent with the experimental results.²⁹ As shown in Figure 8, the bands bend downward due to the electron transfer from the electrode region to the channel area when Ag, Au, and Pt are used as electrode metals.

The coupling between the electrode and the channel region in a FET model can bring two influences. One is the generation of the MIGS in the channel, and the MIGS serve as a reservoir, while the charge transfer among the electrode and the channel, usually resulting in the within-gap Fermi level pinning (FLP).⁵⁹ The other is the modulation of the Fermi level of the relaxed BL Bi₂O₂Se–metal interfacial systems through the formation of the dipole electric field at interface D. The Fermi level modulation can lead to the within- and beyond-gap FLP. As shown in Figure 9b, the Fermi level of the electrode is modulated and lifted above the conduction band of the channel, thus the FLP existing at interface D is attributed to the beyond-gap FLP effect. So, interface D forms the n-type Ohmic contact. The beyond-gap FLP resulting from the Fermi level modulation have been reported at the interfaces of the MoS₂–metal and graphene–metal.^{64,65}

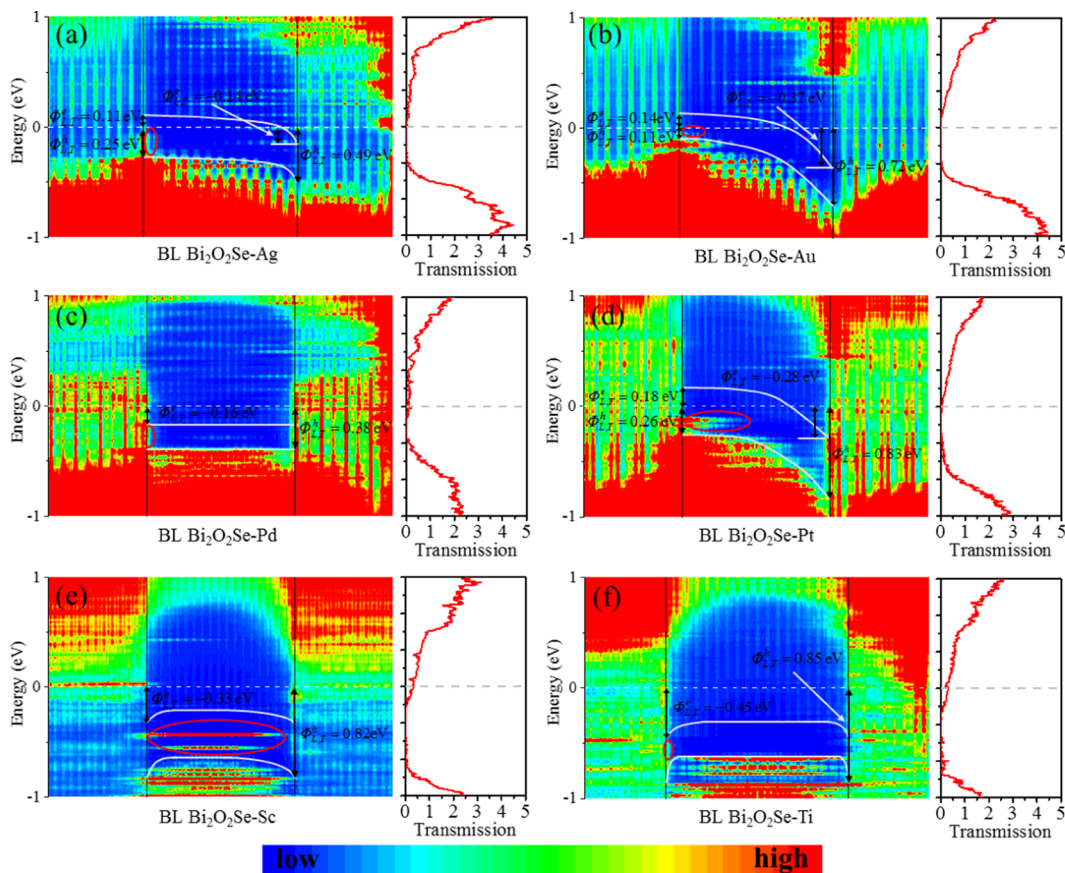


Figure 8. LDDOS and transmission spectrums of the BL Bi₂O₂Se FET with (a) Ag, (b) Au, (c) Pd, (d) Pt, (e) Sc, and (f) Ti electrodes. Solid white lines represent CBM and VBM of BL Bi₂O₂Se in the channel region. White dash lines and gray dashed lines are Fermi levels in LDDOS and transmission spectrums, respectively. $\Phi_{L,T}^e$ represents the electron SBH and $\Phi_{L,T}^h$ stands for the hole SBH in the lateral direction. MIGS at the source–channel interface is circled by the red curves. BL Bi₂O₂Se–metal system and the BL Bi₂O₂Se channel are separated by the upright black lines.

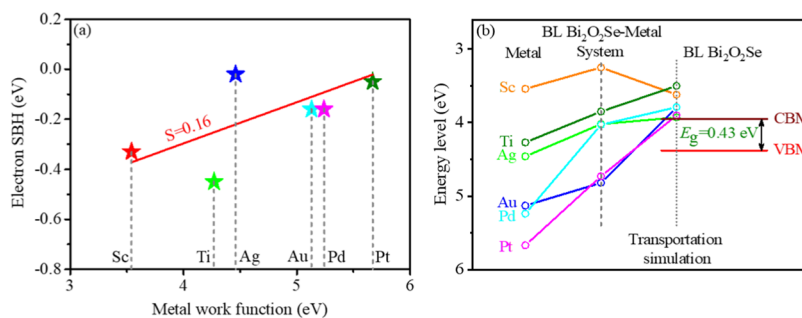


Figure 9. (a) Variation of the lateral electron SBHs in the BL Bi₂O₂Se transistors with the bulk metal work function. S represents the pinning factor that was calculated from the Schottky–Mott rule. (b) Demonstration of Fermi level pinning in the BL Bi₂O₂Se FET. Gray dashed lines and dotted lines, respectively, represent the first and second change of the Fermi level.

The strength of FLP is quantitatively reflected by the pinning factor S , which is obtained from the slope of the fitted red line that depicts the variation of the lateral electron SBH with the work function of the corresponding metal electrode, as shown in Figure 9a. In this definition, $0 \leq S \leq 1$, $S = 0$ means a total FLP and $S = 1$ stands for no FLP at interface D in Figure 2. The fitted S is 0.16 in our investigated BL Bi₂O₂Se FET, which is more smaller than the calculated S in ML MoS₂ FET ($S = 0.27$),⁵² ML black phosphorene FET ($S = 0.28$),¹⁵ ML arsenene FET ($S = 0.33$),^{23,66} and ML blue phosphorene FET ($S = 0.42$).²⁰ The value of $S = 0.16$ indicates that the beyond-gap FLP effect at the interface of the electrode and the

channel region in the BL Bi₂O₂Se transistor is much more intensive than those in the above-mentioned FETs. Because of the consideration of the coupling effect between the electrode and the channel, the quantum transport calculation scheme is more accurate than the WFA process to assess the SBH, especially in a FET that has the strong FLP effect. The beyond-gap FLP effect in the BL Bi₂O₂Se FET is illustrated in Figure 9b.

In a FET, the transport gap E_g^T is defined as the sum of the lateral electron and hole SBH calculated via the quantum transport calculation scheme, that is, $E_g^T = \Phi_{L,T}^e + \Phi_{L,T}^h$. Accordingly, the transport gap E_g^T of the BL Bi₂O₂Se transistor

with Ag, Au, Pd, Pt, Sc, and Ti as electrode metals is 0.35, 0.26, 0.22, 0.50, 0.49, and 0.40, respectively, as demonstrated in Table 1. At the DFT–GGA–PBE level, most of these E_g^T are close to the bandgap (0.43 eV) of intrinsic BL Bi₂O₂Se except for BL Bi₂O₂Se FET with Au and Pd as electrodes due to heavy doping.

4. CONCLUSIONS

In summary, for the first time, we employ two methods, ab initio electronic structure calculations and first-principles quantum transport simulations, to conduct a systematic and comprehensive exploration on the contact properties in BL Bi₂O₂Se FET using Ag, Au, Pd, Pt, Sc, and Ti as electrode metals. The analytic results indicate that the vertical SB (interface B in Figure 2) is absent owing to the strong metallization of BL Bi₂O₂Se on the contact metal. The lateral contact (interface D in Figure 2) is n-type Ohmic for all the checked six metals owing to the intensive beyond-gap FLP at the interface. Furthermore, the formation of the (quasi) Ohmic contact at the interface between BL Bi₂O₂Se and other bulk metal is always expected. The favorable contact properties (Ohmic contact) of BL Bi₂O₂Se with the checked bulk metals make BL Bi₂O₂Se a competitive candidate channel material for using it in the electronic and optoelectronic applications in the upcoming decade.

Our investigation gives a deep insight into the interfacial properties of BL Bi₂O₂Se contacting with Ag, Au, Pd, Pt, Sc, and Ti electrodes in theory, and provides an instruction for the design of BL Bi₂O₂Se-based devices. Interestingly, the latest theoretical investigations reveal that the double-gated monolayer and bilayer Bi₂O₂Se metal-oxide-semiconductor FETs can satisfy the requirements of the International Technology Roadmap for Semiconductors (2013 edition) for high-performance devices.^{67,68} Thus, BL Bi₂O₂Se is deserved to be deeply explored for using it as the channel material of electronic and optoelectronic devices.

AUTHOR INFORMATION

Corresponding Authors

*E-mail: jbyang@pku.edu.cn (J.Y.).

*E-mail: jinglu@pku.edu.cn (J.L.).

ORCID

Lianqiang Xu: 0000-0002-6801-8587

Shiqi Liu: 0000-0002-9166-8254

Xiuying Zhang: 0000-0001-6427-9061

Author Contributions

[†]L.X. and S.L. contributed equally to this work.

Author Contributions

Jinbo Yang and Jing Lu conceived the original idea for the project. Lianqiang Xu and Shiqi Liu carried out the project with the help of Jie Yang, Bowen Shi, Yuanyuan Pan, Xiuying Zhang, Hong Li, Jiahuan Yan, Jingzhen Li, and Linqiang Xu. This manuscript was written by Lianqiang Xu and Shiqi Liu with input from the other authors. All work was supervised by Jinbo Yang and Jing Lu. All authors contributed to the scientific planning and discussions.

Notes

The authors declare no competing financial interest.

ACKNOWLEDGMENTS

This work is financially supported by the Higher School Scientific Research Project of Ningxia Education Department of China (NGY2018-130/Document no. [2014] 222), the Natural Science Foundation of Ningxia of China (No. 2018AAC03236/NZ15262), the key research and development program of Ningxia of China (2018BEE03023), the key Scientific Research Project of Ningxia Normal University of China (No. NXSFZDA1807/NXSFZD1511), and the youth talent support program of Ningxia of China (2016). This paper is also funded by the National Natural Science Foundation of China (No. 11674005/11664026/11704406), the Ministry of Science and Technology of China (No. 2016YFB0700600 (National Materials Genome Project) and 2016YFA0301300).

REFERENCES

- (1) Fiori, G.; Bonaccorso, F.; Iannaccone, G.; Palacios, T.; Neumaier, D.; Seabaugh, A.; Banerjee, S. K.; Colombo, L. Electronics Based on Two-Dimensional Materials. *Nat. Nanotechnol.* **2014**, *9*, 768–779.
- (2) Zeng, M.; Xiao, Y.; Liu, J.; Yang, K.; Fu, L. Exploring Two-Dimensional Materials toward the Next-Generation Circuits: From Monomer Design to Assembly Control. *Chem. Rev.* **2018**, *118*, 6236–6296.
- (3) Zhang, S.; Guo, S.; Chen, Z.; Wang, Y.; Gao, H.; Gómez-Herrero, J.; Ares, P.; Zamora, F.; Zhu, Z.; Zeng, H. Recent Progress in 2d Group-Va Semiconductors: From Theory to Experiment. *Chem. Soc. Rev.* **2018**, *47*, 982–1021.
- (4) Quhe, R.; Li, Q.; Zhang, Q.; Wang, Y.; Zhang, H.; Li, J.; Zhang, X.; Chen, D.; Liu, K.; Ye, Y.; Dai, L.; Pan, F.; Lei, M.; Lu, J. Simulations of Quantum Transport in Sub-5-nm Monolayer Phosphorene Transistors. *Phys. Rev. Appl.* **2018**, *10*, No. 024022.
- (5) Wang, Y.; Huang, P.; Ye, M.; Quhe, R.; Pan, Y.; Zhang, H.; Zhong, H.; Shi, J.; Lu, J. Many-Body Effect, Carrier Mobility, and Device Performance of Hexagonal Arsenene and Antimonene. *Chem. Mater.* **2017**, *29*, 2191–2201.
- (6) Ye, M.; Zhang, D.; Yap, Y. Recent Advances in Electronic and Optoelectronic Devices Based on Two-Dimensional Transition Metal Dichalcogenides. *Electronics* **2017**, *6*, No. 43.
- (7) Sangwan, V. K.; Hersam, M. C. Electronic Transport in Two-Dimensional Materials. *Annu. Rev. Phys. Chem.* **2018**, *69*, 299–325.
- (8) Yoon, Y.; Ganapathi, K.; Salahuddin, S. How Good Can Monolayer MoS₂ Transistors Be? *Nano Lett.* **2011**, *11*, 3768–3773.
- (9) Schwierz, F.; Pezoldt, J.; Granzner, R. Two-Dimensional Materials and Their Prospects in Transistor Electronics. *Nanoscale* **2015**, *7*, 8261–8283.
- (10) Shim, J.; Park, H.-Y.; Kang, D.-H.; Kim, J.-O.; Jo, S.-H.; Park, Y.; Park, J.-H. Electronic and Optoelectronic Devices Based on Two-Dimensional Materials: From Fabrication to Application. *Adv. Electron. Mater.* **2017**, *3*, No. 1600364.
- (11) Akinwande, D.; Petrone, N.; Hone, J. Two-Dimensional Flexible Nanoelectronics. *Nat. Commun.* **2014**, *5*, No. 5678.
- (12) Chhowalla, M.; Jena, D.; Zhang, H. Two-Dimensional Semiconductors for Transistors. *Nat. Rev. Mater.* **2016**, *1*, No. 16052.
- (13) Allain, A.; Kang, J.; Banerjee, K.; Kis, A. Electrical Contacts to Two-Dimensional Semiconductors. *Nat. Mater.* **2015**, *14*, 1195–1205.
- (14) Kang, J.; Liu, W.; Sarkar, D.; Jena, D.; Banerjee, K. Computational Study of Metal Contacts to Monolayer Transition-Metal Dichalcogenide Semiconductors. *Phys. Rev. X* **2014**, *4*, No. 031005.
- (15) Pan, Y.; Wang, Y.; Ye, M.; Quhe, R.; Zhong, H.; Song, Z.; Peng, X.; Yu, D.; Yang, J.; Shi, J.; Lu, J. Monolayer Phosphorene–Metal Contacts. *Chem. Mater.* **2016**, *28*, 2100–2109.
- (16) Jena, D.; Banerjee, K.; Xing, G. H. 2D Crystal Semiconductors: Intimate Contacts. *Nat. Mater.* **2014**, *13*, 1076–1078.

- (17) Park, J. Y.; Cho, J.; Jun, S. C. Review of Contact-Resistance Analysis in Nano-Material. *J. Mech. Sci. Technol.* **2018**, *32*, 539–547.
- (18) Lv, X.; Wei, W.; Zhao, P.; Li, J.; Huang, B.; Dai, Y. Tunable Schottky Contacts in MoSe₂/NbSe₂ (M = Mo and W) Heterostructures and Promising Application Potential in Field-Effect Transistors. *Phys. Chem. Chem. Phys.* **2018**, *20*, 1897–1903.
- (19) Liu, Y.; Guo, J.; Zhu, E.; Liao, L.; Lee, S.-J.; Ding, M.; Shakir, I.; Gambin, V.; Huang, Y.; Duan, X. Approaching the Schottky–Mott Limit in Van Der Waals Metal–Semiconductor Junctions. *Nature* **2018**, *557*, 696–700.
- (20) Li, J.; Sun, X.; Xu, C.; Zhang, X.; Pan, Y.; Ye, M.; Song, Z.; Quhe, R.; Wang, Y.; Zhang, H.; Guo, Y.; Yang, J.; Pan, F.; Lu, J. Electrical Contacts in Monolayer Blue Phosphorene Devices. *Nano Res.* **2018**, *11*, 1834–1849.
- (21) Chen, Z.; Zhang, R.; Yang, J. First-Principles Study on Layered C₂N–Metal Interfaces. *Langmuir* **2018**, *34*, 2647–2653.
- (22) Yang, L.; Charnas, A.; Qiu, G.; Lin, Y.-M.; Lu, C.-C.; Tsai, W.; Paduano, Q.; Snure, M.; Ye, P. D. How Important Is the Metal–Semiconductor Contact for Schottky Barrier Transistors: A Case Study on Few-Layer Black Phosphorus? *ACS Omega* **2017**, *2*, 4173–4179.
- (23) Wang, Y.; Ye, M.; Weng, M.; Li, J.; Zhang, X.; Zhang, H.; Guo, Y.; Pan, Y.; Xiao, L.; Liu, J.; Pan, F.; Lu, J. Electrical Contacts in Monolayer Arsenene Devices. *ACS Appl. Mater. Interfaces* **2017**, *9*, 29273–29284.
- (24) Hao, J.; Jianwei, L.; Langhui, W.; Ying, D.; Yadong, W.; Hong, G. Ohmic Contact in Monolayer Inse-Metal Interface. *2D Mater.* **2017**, *4*, No. 025116.
- (25) Mojtaba, F.; Geert, B. Ohmic Contacts to 2D Semiconductors through Van Der Waals Bonding. *Adv. Electron. Mater.* **2016**, *2*, No. 1500405.
- (26) Liu, Y.; Xiao, H.; Goddard, W. A. Schottky-Barrier-Free Contacts with Two-Dimensional Semiconductors by Surface-Engineered Mxenes. *J. Am. Chem. Soc.* **2016**, *138*, 15853–15856.
- (27) Chuang, H.-J.; Chamlagain, B.; Koehler, M.; Perera, M. M.; Yan, J.; Mandrus, D.; Tománek, D.; Zhou, Z. Low-Resistance 2D/2D Ohmic Contacts: A Universal Approach to High-Performance WSe₂, MoS₂, and MoSe₂ Transistors. *Nano Lett.* **2016**, *16*, 1896–1902.
- (28) Wu, J.; Tan, C.; Tan, Z.; Liu, Y.; Yin, J.; Dang, W.; Wang, M.; Peng, H. Controlled Synthesis of High-Mobility Atomically Thin Bismuth Oxyselenide Crystals. *Nano Lett.* **2017**, *17*, 3021–3026.
- (29) Wu, J.; Yuan, H.; Meng, M.; Chen, C.; Sun, Y.; Chen, Z.; Dang, W.; Tan, C.; Liu, Y.; Yin, J.; Zhou, Y.; Huang, S.; Xu, H. Q.; Cui, Y.; Hwang, H. Y.; Liu, Z.; Chen, Y.; Yan, B.; Peng, H. High Electron Mobility and Quantum Oscillations in Non-Encapsulated Ultrathin Semiconducting Bi₂O₂Se. *Nat. Nanotechnol.* **2017**, *12*, 530–534.
- (30) Zhan, B.; Liu, Y.; Tan, X.; Lan, J.-l.; Lin, Y.-h.; Nan, C.-W. Enhanced Thermoelectric Properties of Bi₂O₂Se Ceramics by Bi Deficiencies. *J. Am. Ceram. Soc.* **2015**, *98*, 2465–2469.
- (31) Pereira, A. L. J.; Santamaría-Pérez, D.; Ruiz-Fuertes, J.; Manjón, F. J.; Cuenca-Gotor, V. P.; Vilaplana, R.; Gomis, O.; Popescu, C.; Muñoz, A.; Rodríguez-Hernández, P.; Segura, A.; Gracia, L.; Beltrán, A.; Ruleova, P.; Drasar, C.; Sans, J. A. Experimental and Theoretical Study of Bi₂O₂Se under Compression. *J. Phys. Chem. C* **2018**, *122*, 8853–8867.
- (32) Chen, C.; Wang, M.; Wu, J.; Fu, H.; Yang, H.; Tian, Z.; Tu, T.; Peng, H.; Sun, Y.; Xu, X.; Jiang, J.; Schröter, Niels, B. M.; Li, Y.; Pei, D.; Liu, S.; Ekahana, S. A.; Yuan, H.; Xue, J.; Li, G.; Jia, J.; Liu, Z.; Yan, B.; Peng, H.; Chen, Y.; et al. Electronic Structures and Unusually Robust Bandgap in an Ultrahigh-Mobility Layered Oxide Semiconductor, Bi₂O₂Se. *Sci. Adv.* **2018**, *4*, No. eaat8355.
- (33) Yu, J.; Sun, Q. Bi₂O₂Se Nanosheet: An Excellent High-Temperature N-Type Thermoelectric Material. *Appl. Phys. Lett.* **2018**, *112*, No. 053901.
- (34) Liu, R.; Lan, J.-L.; Tan, X.; Liu, Y.-c.; Ren, G.-k.; Liu, C.; Zhou, Z.-f.; Nan, C.-w.; Lin, Y.-h. Carrier Concentration Optimization for Thermoelectric Performance Enhancement in N-Type Bi₂O₂Se. *J. Eur. Ceram. Soc.* **2018**, *38*, 2742–2746.
- (35) Liangruksa, M. Effects of Negative Response of Electron Transport to Thermoelectric Properties of Bi₂O₂Se. *Comput. Mater. Sci.* **2016**, *120*, 142–148.
- (36) Li, J.; Wang, Z.; Wen, Y.; Chu, J.; Yin, L.; Cheng, R.; Lei, L.; He, P.; Jiang, C.; Feng, L.; He, J. High-Performance Near-Infrared Photodetector Based on Ultrathin Bi₂O₂Se Nanosheets. *Adv. Funct. Mater.* **2018**, *28*, No. 1706437.
- (37) Yin, J.; Tan, Z.; Hong, H.; Wu, J.; Yuan, H.; Liu, Y.; Chen, C.; Tan, C.; Yao, F.; Li, T.; Chen, Y.; Liu, Z.; Liu, K.; Peng, H. Ultrafast and Highly Sensitive Infrared Photodetectors Based on Two-Dimensional Oxyselenide Crystals. *Nat. Commun.* **2018**, *9*, No. 3311.
- (38) Wu, J.; Liu, Y.; Tan, Z.; Tan, C.; Yin, J.; Li, T.; Tu, T.; Peng, H. Chemical Patterning of High-Mobility Semiconducting 2D Bi₂O₂Se Crystals for Integrated Optoelectronic Devices. *Adv. Mater.* **2017**, *29*, No. 1704060.
- (39) Fu, Q.; Zhu, C.; Zhao, X.; Wang, X.; Chaturvedi, A.; Zhu, C.; Wang, X.; Zeng, Q.; Zhou, J.; Liu, F.; Tay, B. K.; Zhang, H.; Pennycook, S. J.; Liu, Z. Ultrasensitive 2D Bi₂O₂Se Phototransistors on Silicon Substrates. *Adv. Mater.* **2019**, *29*, No. 1804945.
- (40) Wu, M.; Zeng, X. C. Bismuth Oxychalcogenides: A New Class of Ferroelectric/Ferroelastic Materials with Ultra High Mobility. *Nano Lett.* **2017**, *17*, 6309–6314.
- (41) Kresse, G. Ab Initio Molecular Dynamics for Liquid Metals. *J. Non-Cryst. Solids* **1995**, *192–193*, 222–229.
- (42) Kresse, G.; Hafner, J. Ab Initio Molecular Dynamics for Liquid Metals. *Phys. Rev. B* **1993**, *47*, 558–561.
- (43) Kresse, G.; Furthmüller, J. Efficiency of Ab-Initio Total Energy Calculations for Metals and Semiconductors Using a Plane-Wave Basis Set. *Comput. Mater. Sci.* **1996**, *6*, 15–50.
- (44) Kresse, G.; Joubert, D. From Ultrasoft Pseudopotentials to the Projector Augmented-Wave Method. *Phys. Rev. B* **1999**, *59*, 1758–1775.
- (45) Blöchl, P. E. Projector Augmented-Wave Method. *Phys. Rev. B* **1994**, *50*, 17953–17979.
- (46) Perdew, J. P.; Burke, K.; Ernzerhof, M. ERRATA: Generalized Gradient Approximation Made Simple. *Phys. Rev. Lett.* **1997**, *78*, 1396.
- (47) Perdew, J. P.; Burke, K.; Ernzerhof, M. Generalized Gradient Approximation Made Simple. *Phys. Rev. Lett.* **1996**, *77*, 3865–3868.
- (48) Monkhorst, H. J.; Pack, J. D. Special Points for Brillouin-Zone Integrations. *Phys. Rev. B* **1976**, *13*, 5188–5192.
- (49) Bučko, T.; Lebegue, S.; Hafner, J.; Ángyán, J. G. Improved Density Dependent Correction for the Description of London Dispersion Forces. *J. Chem. Theory Comput.* **2013**, *9*, 4293–4299.
- (50) Grimme, S.; Ehrlich, S.; Goerigk, L. Effect of the Damping Function in Dispersion Corrected Density Functional Theory. *J. Comput. Chem.* **2011**, *32*, 1456–1465.
- (51) Grimme, S.; Antony, J.; Ehrlich, S.; Krieg, H. A Consistent and Accurate Ab Initio Parametrization of Density Functional Dispersion Correction (DFT-D) for the 94 Elements H–Pu. *J. Chem. Phys.* **2010**, *132*, No. 154104.
- (52) Zhong, H.; Quhe, R.; Wang, Y.; Ni, Z.; Ye, M.; Song, Z.; Pan, Y.; Yang, J.; Yang, L.; Lei, M.; Shi, J.; Lu, J. Interfacial Properties of Monolayer and Bilayer MoS₂ Contacts with Metals: Beyond the Energy Band Calculations. *Sci. Rep.* **2016**, *6*, No. 21786.
- (53) Pan, Y.; Li, S.; Ye, M.; Quhe, R.; Song, Z.; Wang, Y.; Zheng, J.; Pan, F.; Guo, W.; Yang, J.; Lu, J. Interfacial Properties of Monolayer MoSe₂–Metal Contacts. *J. Phys. Chem. C* **2016**, *120*, 13063–13070.
- (54) Soler, J. M.; Artacho, E.; Gale, J. D.; García, A.; Junquera, J.; Ordejón, P.; Sánchez-Portal, D. The Siesta Method for Ab Initio Order-N Materials Simulation. *J. Phys.: Condens. Matter* **2002**, *14*, 2745–2779.
- (55) Smith, D. R.; Schultz, S.; Markoš, P.; Soukoulis, C. Determination of Effective Permittivity and Permeability of Metamaterials from Reflection and Transmission Coefficients. *Phys. Rev. B* **2002**, *65*, No. 195104.
- (56) Brandbyge, M.; Mozos, J.-L.; Ordejón, P.; Taylor, J.; Stokbro, K. Density-Functional Method for Nonequilibrium Electron Transport. *Phys. Rev. B* **2002**, *65*, No. 165401.

(57) Kim, W. Y.; Kim, K. S. Carbon Nanotube, Graphene, Nanowire, and Molecule-Based Electron and Spin Transport Phenomena Using the Nonequilibrium Green's Function Method at the Level of First Principles Theory. *J. Comput. Chem.* **2008**, *29*, 1073–1083.

(58) Quhe, R.; Feng, S.; Lu, J.; Lei, M. Electronic Properties of Layered Phosphorus Heterostructures. *Phys. Chem. Chem. Phys.* **2017**, *19*, 1229–1235.

(59) Liu, S.; Li, J.; Shi, B.; Zhang, X.; Pan, Y.; Ye, M.; Quhe, R.; Wang, Y.; Zhang, H.; Yan, J.; Xu, L.; Guo, Y.; Pan, F.; Lu, J. Gate-Tunable Interfacial Properties of in-Plane ML MX₂ 1T'-2H Heterojunctions. *J. Mater. Chem. C* **2018**, *6*, 5651–5661.

(60) Liang, Y.; Yang, L. Carrier Plasmon Induced Nonlinear Band Gap Renormalization in Two-Dimensional Semiconductors. *Phys. Rev. Lett.* **2015**, *114*, No. 063001.

(61) Zhang, X.; Pan, Y.; Ye, M.; Quhe, R.; Wang, Y.; Guo, Y.; Zhang, H.; Dan, Y.; Song, Z.; Li, J.; Yang, J.; Guo, W.; Lu, J. Three-Layer Phosphorene-Metal Interfaces. *Nano Res.* **2018**, *11*, 707–721.

(62) Pan, Y.; Dan, Y.; Wang, Y.; Ye, M.; Zhang, H.; Quhe, R.; Zhang, X.; Li, J.; Guo, W.; Yang, L.; Lu, J. Schottky Barriers in Bilayer Phosphorene Transistors. *ACS Appl. Mater. Interfaces* **2017**, *9*, 12694–12705.

(63) Das, S.; Zhang, W.; Demarteau, M.; Hoffmann, A.; Dubey, M.; Roelofs, A. Tunable Transport Gap in Phosphorene. *Nano Lett.* **2014**, *14*, 5733–5739.

(64) Gong, C.; Colombo, L.; Wallace, R. M.; Cho, K. The Unusual Mechanism of Partial Fermi Level Pinning at Metal–MoS₂ Interfaces. *Nano Lett.* **2014**, *14*, 1714–1720.

(65) Zheng, J.; Wang, Y.; Wang, L.; Quhe, R.; Ni, Z.; Mei, W. N.; Gao, Z.; Yu, D.; Shi, J.; Lu, J. Interfacial Properties of Bilayer and Trilayer Graphene on Metal Substrates. *Sci. Rep.* **2013**, *3*, No. 2081.

(66) Guo, Y.; Liu, D.; Robertson, J. 3D Behavior of Schottky Barriers of 2D Transition-Metal Dichalcogenides. *ACS Appl. Mater. Interfaces* **2015**, *7*, 25709–25715.

(67) Quhe, R.; Liu, J.; Wu, J.; Yang, J.; Wang, Y.; Li, Q.; Li, T.; Guo, Y.; Yang, J.; Peng, H.; Lei, M.; Lu, J. High-performance Sub-10 nm Monolayer Bi₂O₂Se Transistors. *Nanoscale* **2019**, *11*, 532–540.

(68) Yang, J.; Quhe, R.; Li, Q.; Liu, S.; Xu, L.; Pan, Y.; Zhang, H.; Zhang, X.; Li, J.; Yan, J.; Shi, B.; Pang, H.; Xu, L.; Zhang, Z.; Lu, J.; Yang, J. Sub 10 nm Bilayer Bi₂O₂Se Transistors. *Adv. Electron. Mater.* **2019**, *5*, No. 1800720.